Supplemental Information for "Ga$_4$C-family crystals, a new generation of star thermoelectric materials, induced by band degeneracies, valley anisotropy, strong phonon scattering and others"

Ao Lou[a], Hua-Hua Fu[a,b,*] and Ruqian Wu[c]

[a]**School of Physics and Wuhan National High Magnetic field center, Huazhong University of Science and Technology, Wuhan 430074, Peoples Republic of China.**

[b]**Institute for Quantum Science and Engineering, Huazhong University of Science and Technology, Wuhan, Hubei, 430074, People's Republic of China.**

[c]**Department of Physics and Astronomy, University of California, Irvine, California 92697-4575, United States.**

A. Electronic band structures and Fermi surface

The electronic band structure of Ga$_4$C calculated by PBE functional (dotted red lines) and HSE06 functional (black lines) are shown in Fig. S1(a) and the Fermi surface below the valence band maximum of 0.1 eV are also plotted in Fig. S1(b). The band gap at PBE level are 0.8 eV which is below the 1.30 eV at HSE06 functional and the four-corners-star shape of the Fermi surface of Ga$_4$C are associated with the flat band along X-W direction.
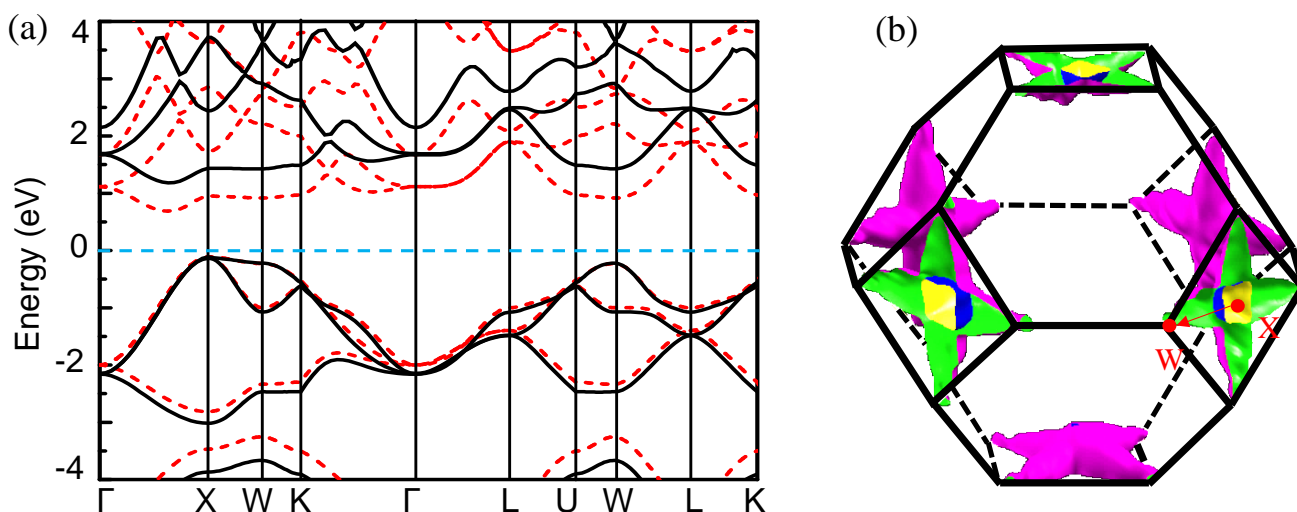

FIG. S1. (a) Electronic band structures of Ga$_4$C calculated by PBE approximation (red dotted lines) and by HSE06 approximation (black solid lines). (b) The Fermi surface below valence band maximum of 0.1 eV. The two high-symmetry points X and W in the first Brillouin zone are marked, and between two points, the connecting bands show flat-band characteristics, which are beneficial to induce a large Seebeck coefficient.

B. Boltzmann transport equation to calculate Lattice thermal conductivity

The lattice thermal properties of all supertetrahedral Ga$_4$C samples are simulated by solving the linear Boltzmann transport equation (BTE) iteratively considering three-phonon scattering process[1,2]. The lattice thermal conductivity k_{latt} can be expressed by the sum of contributions over all the phonon modes λ as below,

$$k_{latt} = \frac{1}{NV\kappa_B T^2} \sum_\lambda (\hbar\omega_\lambda)^2 f_0(f_0 + 1)\nu_\lambda^\alpha \nu_\lambda^\beta, \tag{1}$$

where N is the number of wave vectors included in the first BZ, V is volume of the crystallographic unit cell, ω_λ is the angular frequency corresponding to a phonon mode λ, f_0 is the equilibrium Bose-Einstein distribution function and v_λ is the phonon group velocity which is determined by $v_\lambda = \frac{1}{\hbar}\frac{\partial \varepsilon_{i,k}}{\partial k_\lambda}$. The linearized BTE of F_λ^β can be written as $F_\lambda = \tau_\lambda^0(v_\lambda + \Delta_\lambda)$, in which τ_λ^0 denotes the relaxation time which can be obtained by the three-phonon

transition probabilities $\sum_{\lambda'\lambda''}^{\pm}\Gamma_{\lambda\lambda'\lambda''}^{\pm}$ summed with the corresponding isotopic disorder term $\sum_{\lambda'}^{-}\Gamma_{\lambda'\lambda''}$ described in the followings,

$$\frac{1}{\tau_\lambda^0} = \frac{1}{N}\left\{\sum_{\lambda'\lambda''}^{+}\Gamma_{\lambda'\lambda''\lambda'''}^{+} + \sum_{\lambda'\lambda''}^{-}\frac{1}{2}\Gamma_{\lambda\lambda'\lambda''}^{-} + \sum_{\lambda'}^{-}\Gamma_{\lambda\lambda'}\right\}, \tag{2}$$

$$\Gamma_{\lambda\lambda'\lambda''}^{S} = \frac{\hbar\pi\varphi_1\varphi_2}{4\omega_\lambda\omega_{\lambda'}\omega_{\lambda''}}|V_{\lambda\lambda''\lambda'''}^{\pm}|^2, \tag{3}$$

$$\sum_{\lambda'}\Gamma_{\lambda\lambda'} = \frac{\pi\omega^2}{2}\sum_{i}g(i)|e_\lambda^*(i)\cdot e_{\lambda'}^*(i)|^2\delta(\omega_\lambda - \omega_{\lambda'}). \tag{4}$$

Note that in Eq. (12), the index S indicates + or -, corresponding to the absorption or the emission process. For $S = +$, $\varphi_1 = (f_0' - f_0'')$ and $\varphi_2 = \delta(\omega_\lambda + \omega_{\lambda'} - \omega_{\lambda'})$, while for $S = -$, $\varphi_1 = (f_0' + f_0'' + 1)$ and $\varphi_2 = \delta(\omega_\lambda - \omega_{\lambda'} - \omega_{\lambda'})$. The scattering matrix elements $V_{\lambda\lambda'\lambda''}^{\pm}$ are associated with the anharmonic force constants (FCs), which can be obtained from DFT calculations. Moreover, the anharmonic FCs are obtained by using the Phonopy package[3] with a finite-displacement step of 0.01Å. To perform the numerical calculations, a $3 \times 3 \times 3$ supercell and a cutoff radius of 0.6 nm are adopted, and the q-point mesh is employed $19 \times 19 \times 19$ to obtain a converged lattice thermal conductivity as implemented in ShengBTE package[4].

By applying the Boltzmann transport equations to calculate the electronic transport properties and the lattice thermal conductivity, the Seebeck coefficient S, electric conductivity σ, the thermal conductivity κ including the electrons' thermal conductivity κ_e and the lattice thermal conductivity κ_L, and the power factor $S^2\sigma$ in some n-type doping Ga_4C versus temperature are calculated and shown in Fig. S2(a)-(d). Moreover, Fig. S2(e), (f) and (g) show the transport coefficients in three vertical directions (i.e., xx, yy and zz directions). Their nearly same values demonstrate the isotropic properties of thermoelectric performance of Ga_4C.
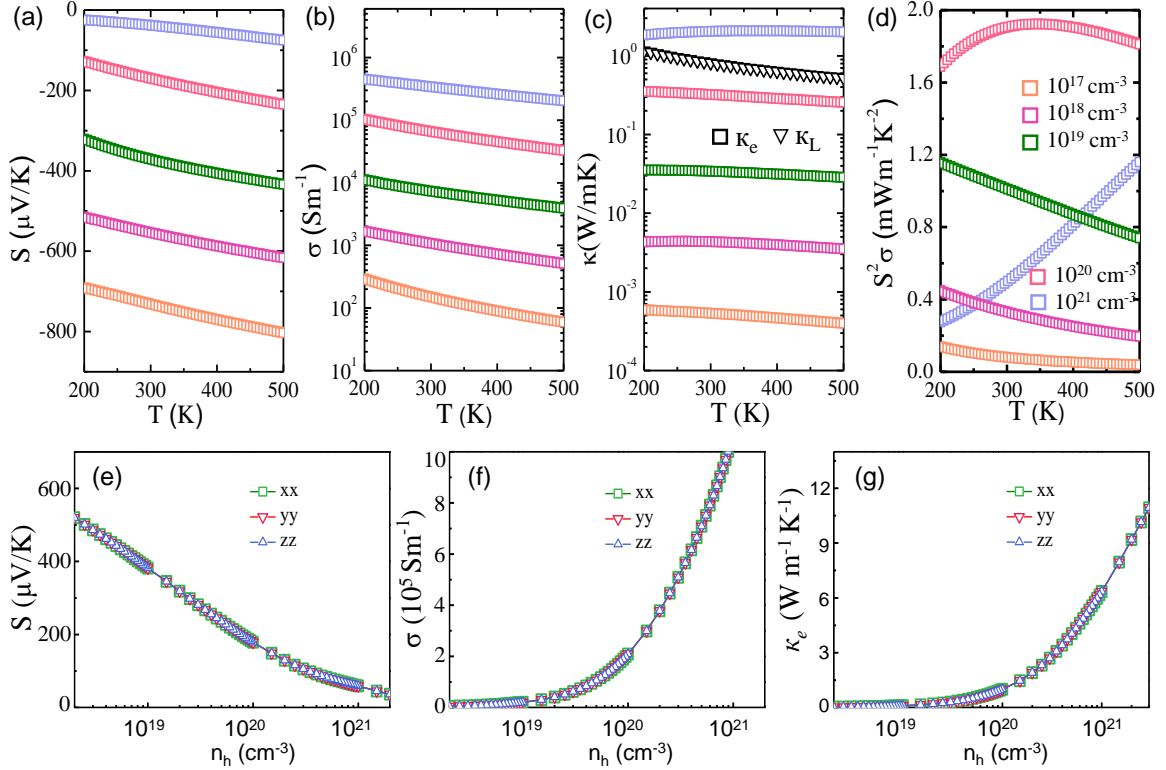

FIG. S2. Electronic transport properties of Ga_4C as a function of temperature and n-type carrier concentration. (a) the Seebeck coefficient S, (b) the electric conductivity σ, (c) the thermal conductivity κ and (d) the power factor $S^2\sigma$ versus the temperature T. In (c), κ_e and κ_L denote the electronic and phononic thermal conductivity, respectively. Moreover, the Seebeck coefficient (e), the electric conductance (f) and the electrons' thermal conductance (g) along three axis directions, i.e., xx-, yy- and zz-directions, respectively.

C. Inter-valley scattering mechanism in the four band configurations

In this subsection, we present some other numerical results on the electronic band structures and scattering rates in the different band configurations of Ga_4C. Figure S3 shows the electronic band structures with the different effective masses designed in the particular bands along the high-symmetry path X-W. In our calculations, the initial band denotes the original band with any modification, Case I, Case II and Case III refer to the modified band along the W-X path with the effective mass 0.0459, 0.0326 and 0.0249 m_e.

As described in the main context, the both approximation approaches draw the same conclusion that among the four band configurations, the original flat bands contribute to exhibit the largest values of PF, S, μ_W and m_{DOS}, although σ and μ may be weaker in the original band configuration. To understand the underlying physical mechanism responsible for the above-mentioned thermoelectric phenomena, we should consider further the altered inter-valley carriers' scattering, as demonstrated in Fig. S4, where the hole scattering from ADP, POP and IMP are given separately for the original flat band and the modified band in Case III for comparison. The dashed lines denote the single-parabolic-band cutoff energy corresponding to the Fermi level at about -0.085 eV. It is clear that the large reduction of σ and μ can be traced to the portion increasing in the POP scattering in comparison with the light band in Case II.

Note that the POP scattering is described by $\tau_{POP}^{-1} \propto |k-k'|^{-2}$, and characteristically intensifies with the proximity of the initial and the final states in the reciprocal space[6]. The distance between two neighboring valleys is eliminated, due to the transformation of the flat belt connecting the two valleys, when the doping concentration adjusts the Fermi level to -0.085 eV and enter the second valley, the inter-valley scattering is obviously enhanced. The obvious difference is that when we make the two connected valleys independent, as seen light band, the inter-valley scattering tends to be normal. Although this flat band produces stronger inter-valley scattering, it compensates for the decrease in conductivity due to its large effective mass, resulting in higher thermoelectric performance.
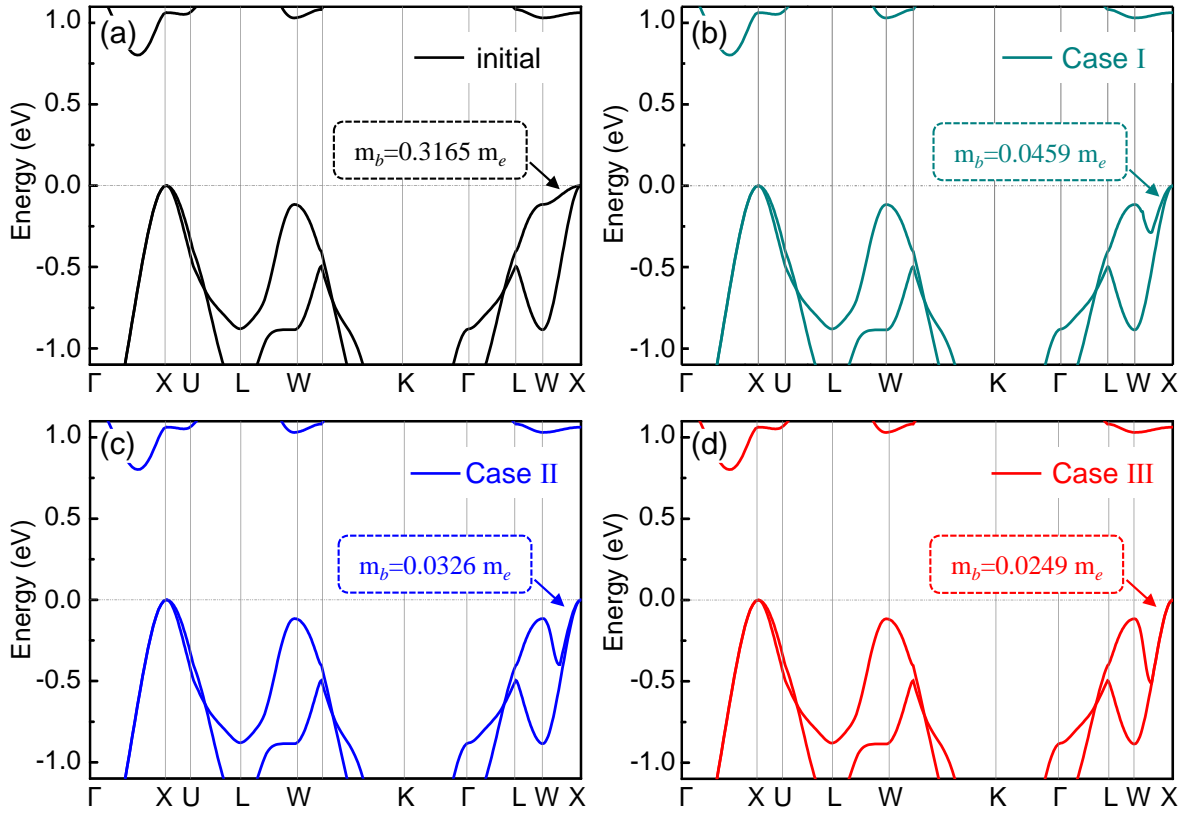
FIG. S3. (a) Electronic band structures of the crystal Ga$_4$C samples calculated with PBE. The band along the W-X path neat the Fermi level is modified to manipulate the electronic valley located at the high-symmetry points W and X, and by designing the different band slopes in them to realize three particular bands with the large effective mass 0.024 m$_e$ in (b), middle effective mass in 0.017 m$_e$ in (c) and small effective mass 0.013 m$_e$ in (d). For a comparison study, the band structure of the original configuration (initial) is also provided here.
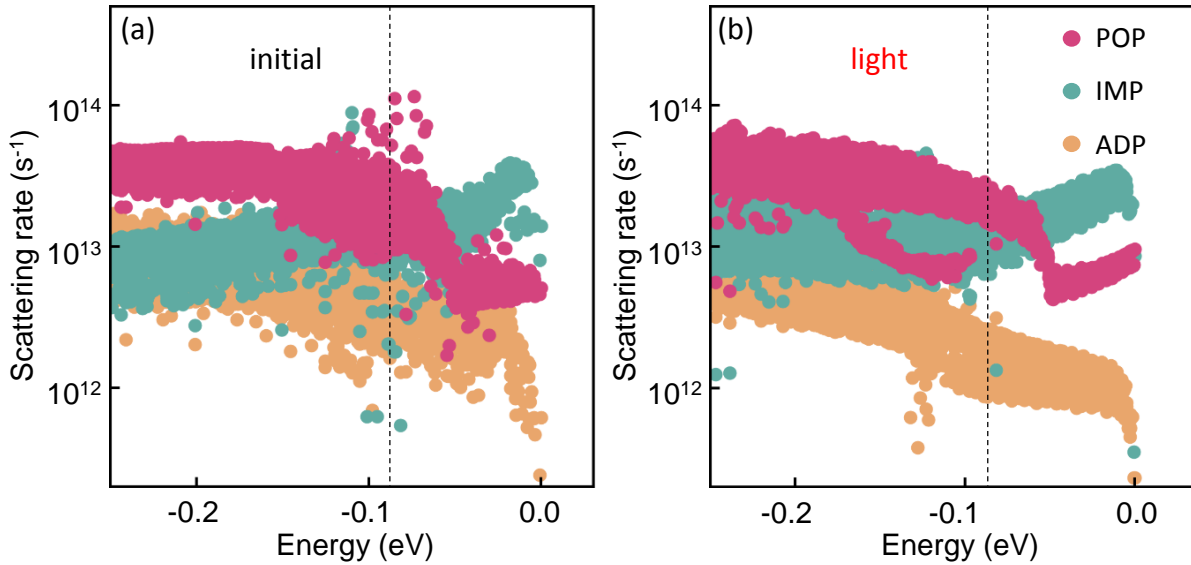

FIG. S4. The ab initio hole scattering rates with respect to different carrier energies for the two different band structure models. (a) and (b) denote the numerical results for the initial and light band structure model, respectively.

D. How to calculate the weighted mobility and the DOS effective mass m$_{DOS}$

The weighted mobility μ_W is an important parameter to evaluate the electrons' transport properties. μ_W is usually obtained further from the electric conductivity σ and the Seebeck coefficient S, as described below[6]:

$$\mu_W = \frac{3\pi^2\sigma}{(2k_BT)^{\frac{3}{2}}}\left[\frac{\exp(\frac{|S|}{k_B}-2)}{1+\exp(-5(\frac{|S|}{k_B}-1))} + \frac{\frac{3|S|}{\pi^2 k_B}}{1+\exp(5(\frac{|S|}{k_B}-1))}\right], \tag{5}$$

by which account, the DOS effective mass m_{DOS} is given by

$$m_{DOS} = \left(\frac{3\pi^2 n}{(2k_BT)^{\frac{3}{2}}}\left[\frac{\exp(\frac{|S|}{k_B}-2)}{1+\exp(-5(\frac{|S|}{k_B}-1))} + \frac{\frac{3|S|}{\pi^2 k_B}}{1+\exp(5(\frac{|S|}{k_B}-1))}\right]\right)^{\frac{2}{3}}, \tag{6}$$

where k_B is Boltzmann's constant and n is carrier concentration. These relations render μ_W and m_{DOS} doping-independent in the non-degenerate regime so long as scattering is also doping-independent.

E. Pair-correlation function for the crystal Ga$_4$C at the temperature 650 K

In this subsection, we turn to examine the possible melting temperature of the crystal Ga$_4$C. By using molecular dynamics simulation, we calculated the pair-correlation function (PCF) for the crystal Ga$_4$C at temperature 650 K as illustrated in the following figure (see Fig. 5). One may find that PCF for the temperature 650 K still demonstrates the presence of long-range order in the arrangement of atoms typical of a crystal. That is to say that up to the temperature 650 K, this material sample remains in a good solid state.
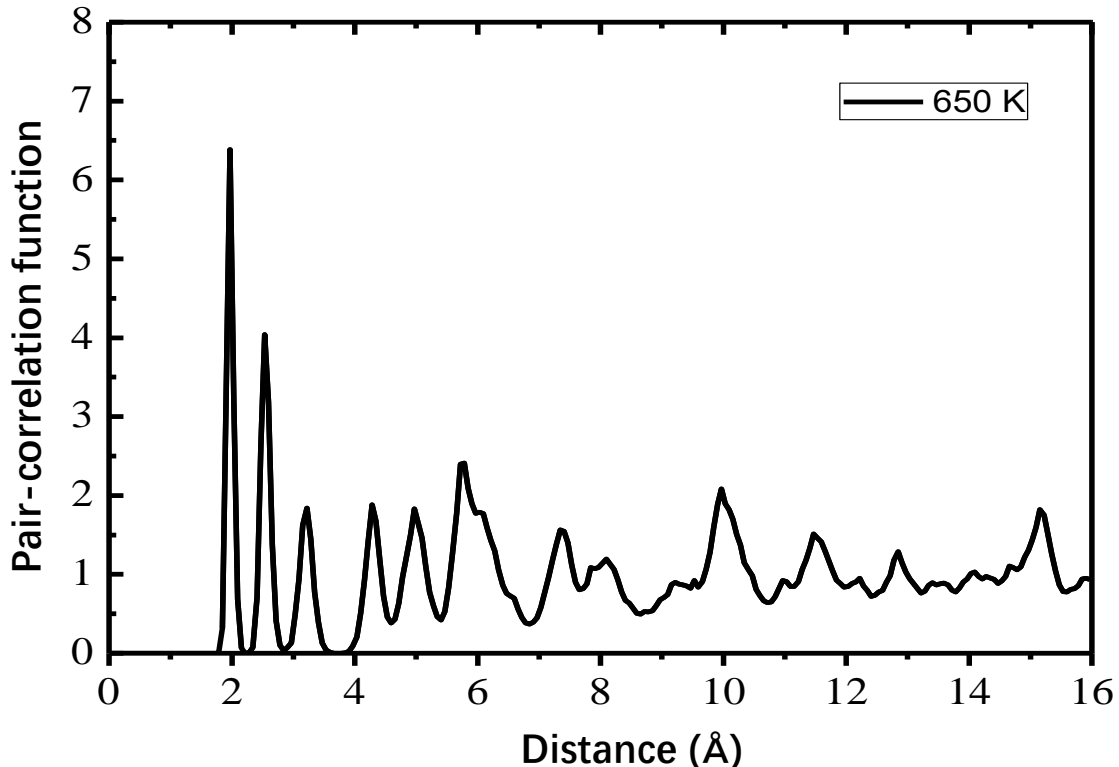

FIG. S5. Pair-correlation function for the crystal Ga4C from molecular dynamics simulation at temperature 650 K. The graph corresponds to a time point of 10 ps from the start of the simulation.

F. Band structures and thermoelectric properties of Ga$_4$C under different tensile strains

In the main context, we applied the tensile strain engineering as an effective way and further to decrease the lattice thermal conductivity. To demonstrate the influence of tensile strain on the electronic properties of Ga$_4$C, we calculated the electronic band structures of Ga$_4$C with the tensile strain ratio 0.25%, 0.50% and 0.75%, and present the numerical results in Fig. S6, where the band structure of the original sample (without any strain) is also provided for comparison. One can see that the electronic band structures, especially the flat bands and the band degeneracies near the Fermi level, hardly show any changes, indicating that the tensile strain engineer doesn't modify the electronic properties of Ga$_4$C.

Furthermore, the power factor under the constant-relaxation-time approach (CRT) and the polarized-optical-phonon-scattering (POP) mechanism, and the phononic dispersions of the crystal Ga$_4$C under different tensile strain ratios 0.0%, 0.25%, 0.50% and 0.75% are also calculated and provided in Fig. S7(a) and S7(b), respectively. One can see that although the electronic band structures do not change significantly under different tensile strain ratios, the power factor obtained by POP scattering decreases clearly as the tensile strain is enhanced (see Fig. S7(b)). Moreover, under the different tensile strain, the all phononic dispersions don't show any virtual frequencies as shown in Fig. S8, enuring the dynamic stabilities of all material samples under tensile strain. However, the optical branches move downward obviously as the tensile strain is enhanced, which is much different from the electronic band structures under the tensile strain as displayed in Fig. S6, which can be used to understand the decreasing power factor drawn in Fig. S7.

In order to understand the underlying physical mechanisms for the thermoelectric behavior that the lattice thermal conductivity decreases with the increasing of tensile strain, the corresponding thermal conductivity parameters under different tensile strain ratios 0.0%, 0.25%, 0.50% and 0.75% are also studied here. Figure S9(a) and S9(b) show the cumulative normalized κ_l and its differential, respectively. One can find that the contribution of optical branch to lattice thermal conductivity increases with the increasing of tensile strain. Moreover, the decreasing lattice thermal conductivity is attributed to the enhancement of phonon scattering in low-frequency acoustic bands, rather than the phonon group velocity, as illustrated in Figs. S9(c) and S9(d), which can be interpreted by the strengthened coupling between acoustic and optical branches and the expanded phase space of phonon-phonon scattering.
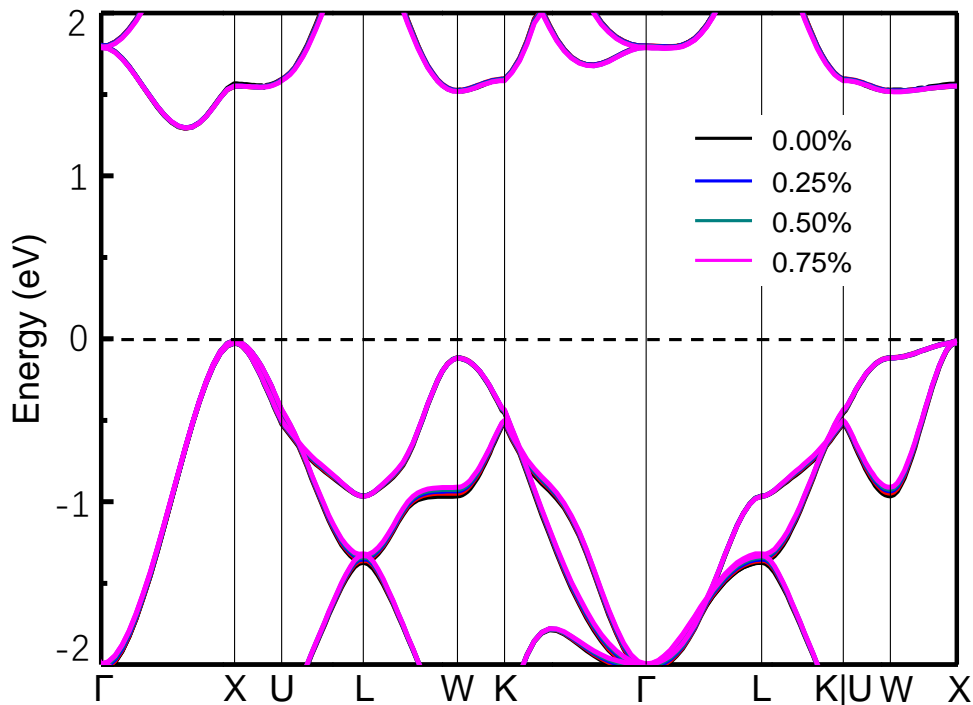

FIG. S6. Electronic band structure of Ga$_4$C calculated with HSE06 under strains compared with the initial band structure. The tensile strain ratio is set as 0.5%, 0.75% and 1.0%. At the low strain, there is no significant change in band structure, indicating that there is no band convergence occurs and that the thermoelectric properties will not be enhanced under constant relaxation time.
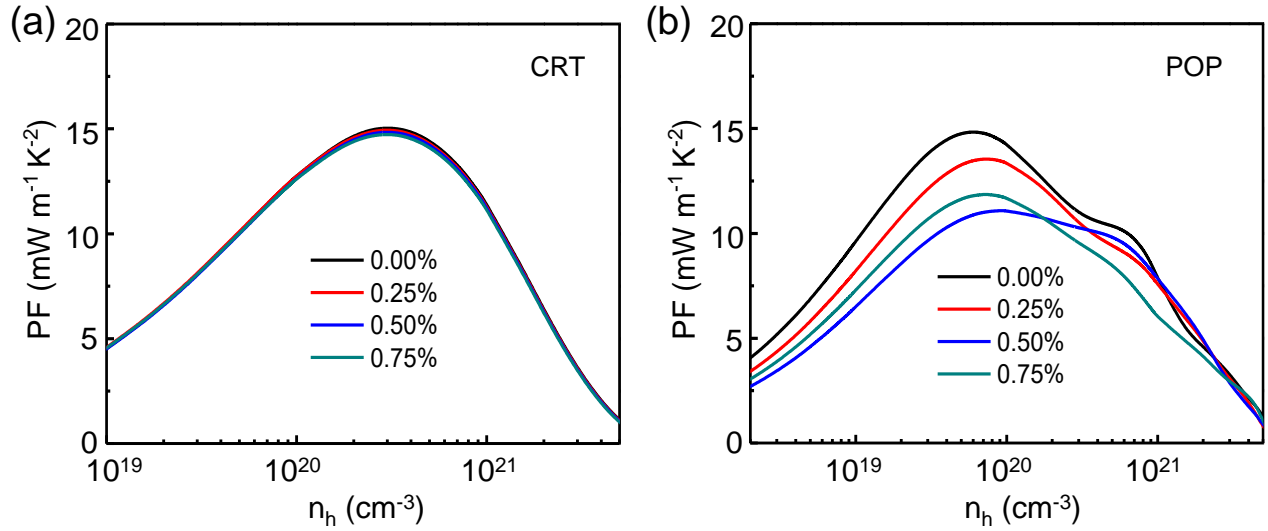
FIG. S7. The power factor are calculated from (a) constant relaxation time approach (CRT) and (b) polarized optical phonon scattering (POP) mechanism are given separately under the tensile strain ratio 0.00%, 0.25%, 0.50% and 0.75%. The PW under CRT approach don't change significantly, however, POP scattering results in a significant decrease in PW as the tensile strain is enhanced.
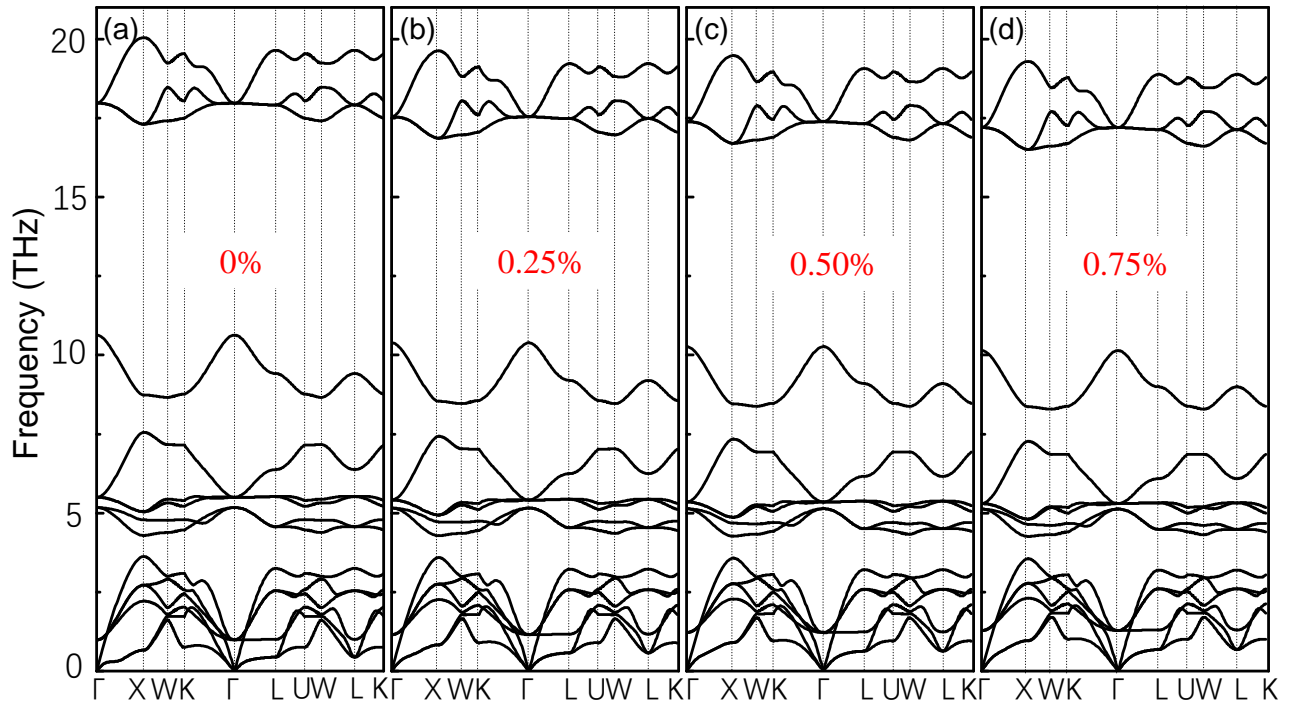

FIG. S8. The phonon dispersions of the crystal Ga_4C under different tensile strain ratios 0.0%, 0.25%, 0.50% and 0.75% in the figure (a)-(d), respectively, where the optical branches decrease gradually while the acoustic branches gradually harden with the increasing tensile strain.
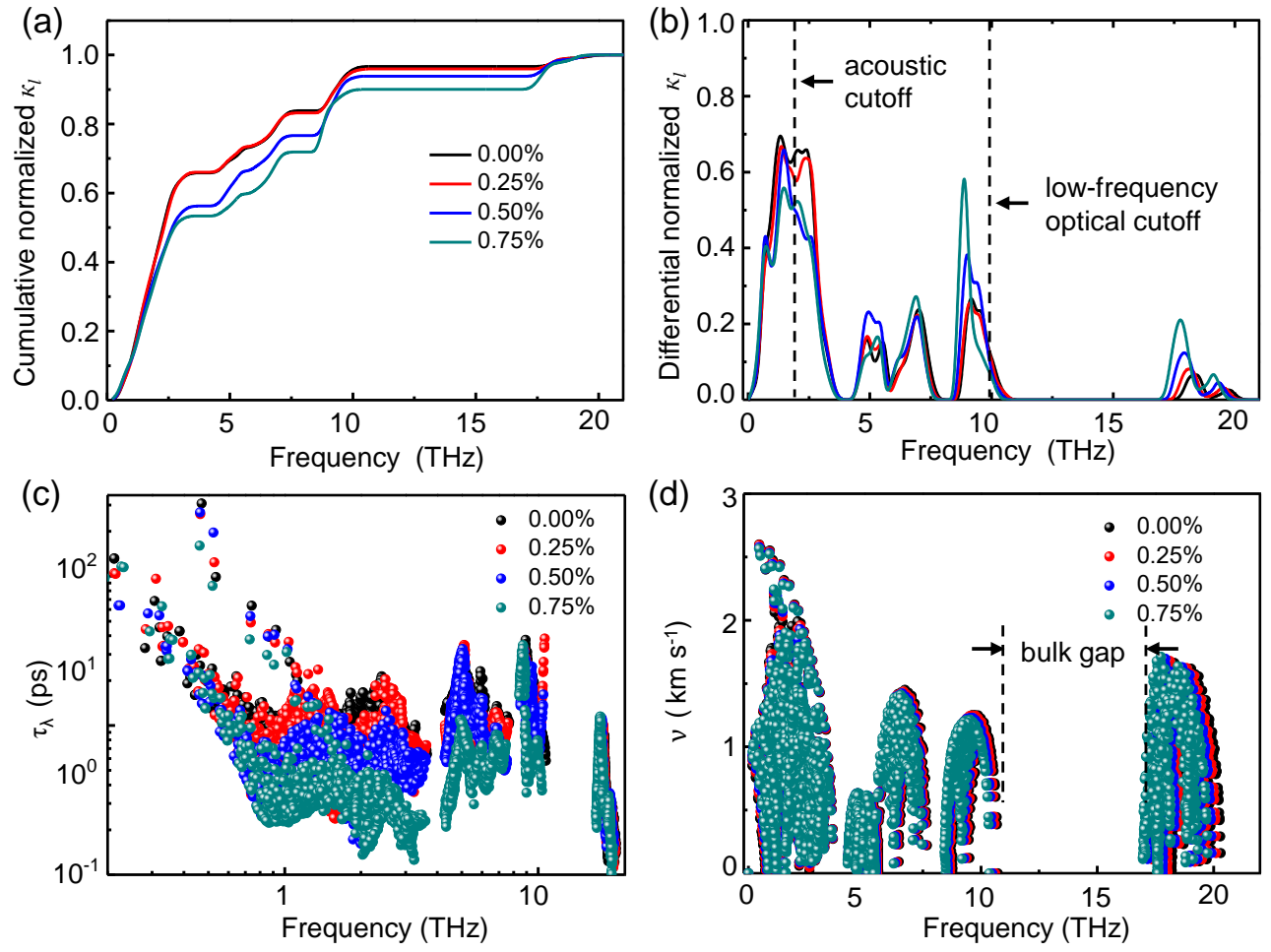
FIG. S9. The thermal conductivity and phononic scattering time, phonon group velocity under different tensile strain ratios 0.0%, 0.25%, 0.25% and 0.75%. (a) and (b) Cumulative and differential of normalized κ_l. (c) and (d) Phonon lifetime τ_λ and group velocity ν versus the phonon frequency.

G. Electron and phonon structures of Ga_4C-family materials

The electron and phonon structures of the Ga4C-family materials including X_4Y (X = B, Al, and Y = C, Si), are provided in Fig. S10 and Fig. S11, in which the electron and phonon structures of Ga_4C are also provided here for comparison. One can see that their electron and phonon structures are much similar with these of Ga_4C. Especially in Al_4C, the CBM exists at both X and W points and as a result, there is a completely flat band while retaining a small band effective mass along the Γ-X path, which is beneficial for a large power factor[7]. For phonon structures, all compounds show soft acoustic and flat optical branches, indicating low phonon group velocities in them.
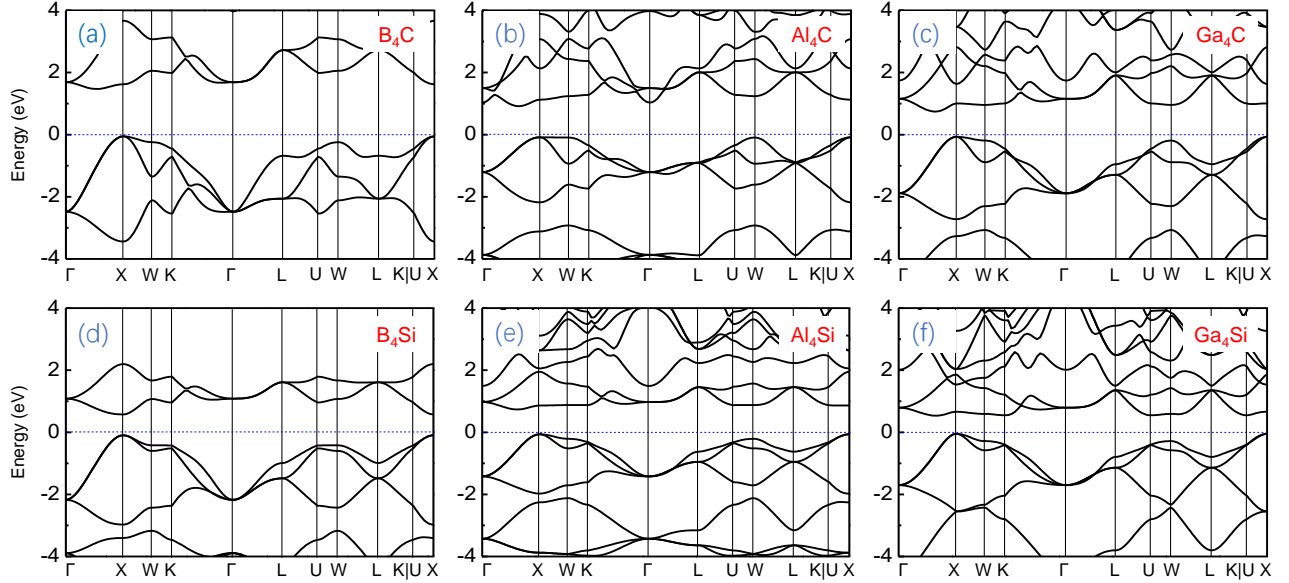

FIG. S10. Electron band structures of X_4Y (X = B, Al, Ga, and Y = C, Si).
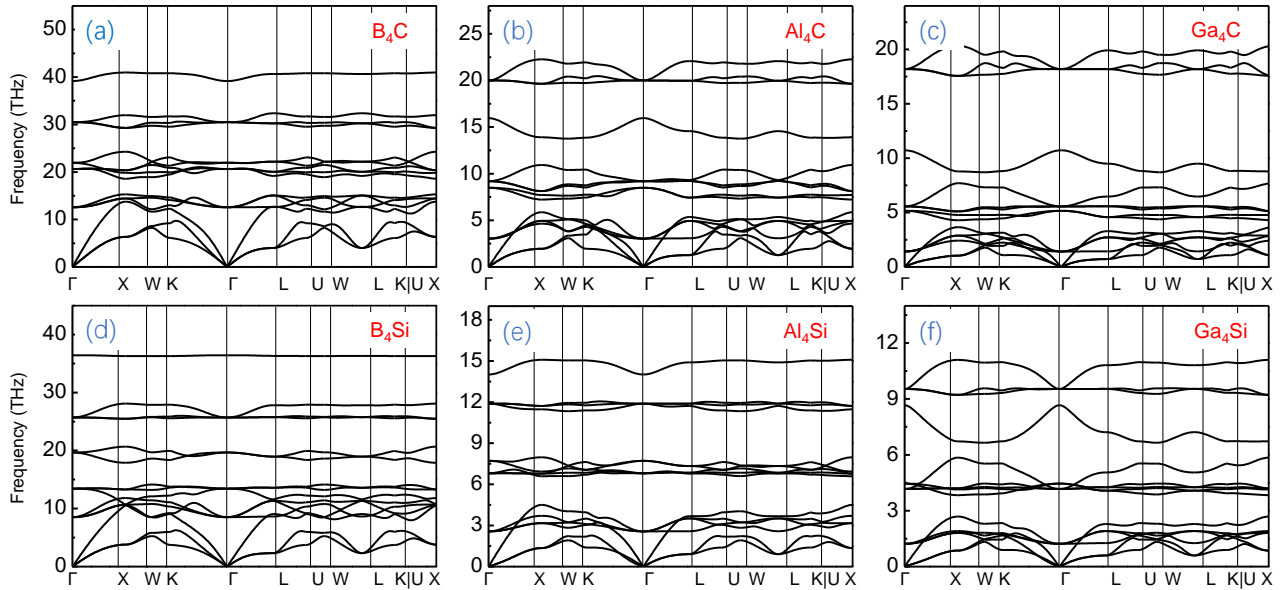

FIG. S11. Phonon band structure of X_4Y (X = B, Al, Ga, and Y = C, Si).

References

1. M. Omini and A. Sparavigna, An iterative approach to the phonon Boltzmann equation in the theory of thermal conductivity, Phys. B: Conden. Matt. **212**, 101 (1995).
2. M. Omini and A. Sparavigna, Beyond the isotropic-model approximation in the theory of thermal conductivity, Phys. Rev. B **53**, 9064 (1996).
3. A. Togo and I. Tanaka, First principles phonon calculations in materials science, Scr. Mater. **108**, 1 (2015).
4. W. Li, J. Carrete, N. A. Katcho, and N. Minggo, ShengBTE: A solver of the Boltzmann transport equation for phonons, Comput. Phys. Commun. **185**, 1747 (2014).
5. G. J. Snyder, A. H. Snyder, M. W. Wood, R. Gurunathan, B. H. Snyder, and C. -N. Chang, Weighted Mobility, Adv. Mater. **32**, 2001537 (2020).
6. P. Junsoo, D. Maxwell, X. Yi, W. Max, G. J. Snyder, and A. Jain, When band convergence is not beneficial for thermoelectrics, Nature commun. **12**, 3425 (2021).
7. D. I. Bilco, G. Hautier, D. Waroquiers, G. M. Rignanese, and P. Ghosez, Low-Dimensional transport and large thermoelectric power factors in bulk semiconductors by band engineering of highly directional electronic states, Phy. Rev. Lett. **114**, 136601 (2015).